JOURNAL OF GEOPHYSICAL RESEARCH, VOL. 111, D14209, doi:10.1029/2005JD006955, 2006

Remote sensing of stratocumulus clouds: Uncertainties and biases due to inhomogeneity

T. Zinner[1] and B. Mayer[1]

Received 5 December 2005; revised 14 March 2006; accepted 18 April 2006; published 26 July 2006.

[1] Standard cloud remote sensing techniques rely on two basic assumptions: First, clouds are assumed to be plane-parallel and homogeneous within each satellite pixel. Second, pixels are assumed independent and the net horizontal radiative transport between pixels is neglected. These assumptions cause considerable uncertainty and bias in the retrieval of cloud properties, which depend on the sensors spatial resolution as well as the illumination and observation geometry. The errors are quantified for several typical sensor settings. The basis of the investigation is a data set of high-resolution three-dimensional cloud property distributions of marine stratocumulus obtained from airborne radiance observations. For this predefined cloud data the sensor signals are simulated using a three-dimensional Monte Carlo radiative transfer model. Cloud properties (optical thickness, effective radius) are retrieved for the simulated observations using a two-channel retrieval, which are then compared to the given cloud data. For the retrieval of the optical thickness the main findings are large uncertainty of individual pixel values occurs for a high spatial resolution (e.g., airborne sensors) due to nonnegligible horizontal photon transport at this pixel size. For the typical polar-orbiting and geostationary sensor settings the neglect of subpixel inhomogeneity takes effect as well. Nonetheless, biases are generally small within ±5%, if pixels are overcast. If this is not guaranteed, the bias grows rapidly, for example, to typical underestimations of 20% and more for a geostationary sensor. For the retrieval of effective radius values are generally found to be about 5% larger than expected for idealized homogeneous plane-parallel cloud conditions.

Citation: Zinner, T., and B. Mayer (2006), Remote sensing of stratocumulus clouds: Uncertainties and biases due to inhomogeneity, *J. Geophys. Res.*, *111*, D14209, doi:10.1029/2005JD006955.

1. Introduction

[2] On average about 70% of the Earth's surface is covered with clouds [*Rossow and Schiffer*, 1999]. Clouds are the key controlling factor of the Earth's radiation budget and the observation of their characteristics and evolution on a global scale is an important task of satellite based remote sensing. Still, this task is almost exclusively covered by passive remote sensing techniques as only these can provide sufficiently complete data sets in terms of horizontal coverage. Satellite cloud instruments have typical horizontal resolutions of several hundred meters to several kilometers. The three-dimensional character of clouds and their inhomogeneity on all scales of space and time hampers the determination of cloud properties from reflected radiance.

[3] Below the sensor's field of view, cloud inhomogeneity remains unknown. Standard remote sensing techniques assume that clouds are plane-parallel and homogeneous within each satellite pixel, the so-called plane parallel approximation (PPA). This approximation leads to a bias in the retrieved cloud properties due to the nonlinear relationship between cloud properties and the reflected radiance, the so-called plane-parallel bias [*Cahalan et al.*, 1994]. This bias increases with pixel size as the amount of subscale inhomogeneity is increasing. The second assumption generally applied by remote sensing algorithms is the independent pixel approximation (IPA), i.e., the reflected radiance from each individual pixel is considered independent from the surrounding pixels. This neglect of net horizontal transport of radiation between neighboring pixels causes the independent pixel error [*Cahalan et al.*, 1994]. It increases as the pixel size decreases because the smaller the pixel is, the more important becomes the net horizontal photon transport compared to the vertical transport.

[4] Several studies quantified the impact of cloud inhomogeneity and three-dimensional (3-D) radiative transfer on radiative fluxes [e.g., *Cahalan et al.*, 1994; *Marshak et al.*, 1998b; *Fu et al.*, 2000; *Scheirer and Macke*, 2003; *Di Giuseppe and Tompkins*, 2003]. In addition, first attempts have been made to investigate the uncertainties of standard cloud property retrievals [*Loeb et al.*, 1998; *Varnai*, 2000] and to systematically quantify them [*Varnai and Marshak*, 2001]. First approaches to quantitatively consider cloud inhomogeneity and 3-D radiative transfer in retrieval schemes were proposed as well [*Faure et al.*, 2001; *Iwabuchi and Hayasaka*, 2003]. Most of these investigations were based on a-priori defined three-dimensional

[1]Institut für Physik der Atmosphäre, Deutsches Zentrum für Luft- und Raumfahrt, DLR Oberpfaffenhofen, Wessling, Germany.

0148-0227/06/2005JD006955$09.00

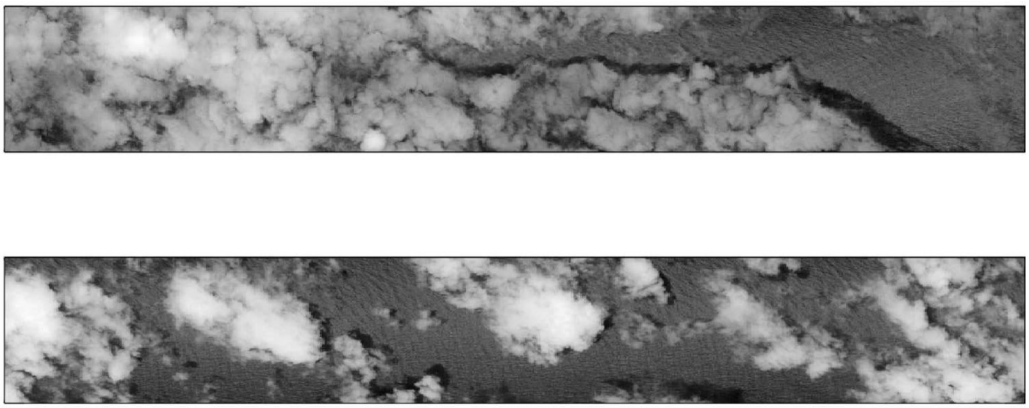

Figure 1. Examples of CASI observations: radiance at 753 nm, horizontal resolution 15 m × 15 m, scene size approximately 1.3 km × 10 km.

cloud structures, 3-D distributions of liquid water content (LWC) and droplet size. The simulation of the associated radiation fields using 1-D or the more realistic 3-D radiative transfer models enables detailed analyses of the performance of remote sensing techniques. For such an analysis the simulated radiance is used as input to standard retrieval methods and the retrieved cloud properties are then directly compared to the underlying cloud structures. Consequently, all results depend on the complexity and the realism of the used cloud structures.

[5] Different approaches were used to generate cloud structures for radiative transfer investigations, for example, physics-based numerical cloud models [e.g., *O'Hirok and Gautier*, 1998; *Wyser et al.*, 2002; *Scheirer and Macke*, 2003] or statistical cloud models [*Cahalan et al.*, 1994; *Evans and Wiscombe*, 2004; *Scheirer and Schmidt*, 2005]. While the cloud resolving numerical models have the advantage of directly generating complete physically consistent cloud structures, the statistical cloud models directly resemble measured cloud characteristics. Disadvantage of the first is the great computational cost and the characteristic damping of small-scale variability for numerical reasons [*Bryan et al.*, 2003]; the statistical reconstruction, on the other hand, has to intricately find sensible solutions to fill the large observational information gaps.

[6] Generally, it seems desirable to stay as close as possible to observed data. The following investigations of the impact of cloud inhomogeneity on the retrieval of cloud properties for several typical air- and satellite-borne sensor settings are based on 3-D cloud structures determined from high-resolution airborne remote sensing observations (Figure 1). *Zinner et al.* [2006] developed a technique for the retrieval of the 3-D structure, taking into account the effect of horizontal photon transport explicitly. The resolution of the observation was high enough to neglect subpixel inhomogeneity. Thus both plane-parallel as well as independent-pixel error are circumvented by this retrieval. Using this method, 27 three-dimensional cloud structures of single layer marine stratocumulus were retrieved from high resolution imagery. These constitute a unique set of cloud structures representative of marine stratocumulus and realistic in a way that each of the 3-D cloud structures best matches the available observation.

[7] This study, as well as most of the above-cited ones, concentrates on marine stratocumulus. First, this boundary layer water cloud type plays an important role in the global radiation budget as about 30% of the Earth's surface is covered by single layer low-level clouds mostly over ocean [*Rossow and Schiffer*, 1999]. Second, this comparatively simple cloud type allows to separate the effect of inhomogeneity from other complications like multilayered clouds, cloud particle phase, and shape effects, or the influence of surface albedo. The impact of cloud inhomogeneity on several typical cloud remote sensing resolutions are investigated: a typical airborne sensor resolution, a typical polar-orbiting instrument, and a geostationary satellite sensor setting. Section 2.1 briefly summarizes the method by *Zinner et al.* [2006] as far as it is relevant for the following studies. The radiative transfer model and the simulations are described in section 2.2. Section 2.3 presents the implementation of a standard cloud property retrieval, the subject of the following investigation. The error measures are introduced in section 2.4 before the results are presented in section 3. The paper is wrapped up by the discussion and conclusion sections.

2. Methods

2.1. Cloud Data

[8] The three-dimensional cloud structures constituting the experimental environment for the following simulations of solar radiative transfer and remote sensing are determined from high horizontal resolution radiance observations (Figure 1). The radiance data was observed by the compact airborne spectrographic imager (CASI) [*Babey and Anger*, 1989] on board the DLR Do-228 aircraft during the ACE2 CLOUDYCOLUMN campaign over large-scale marine stratocumulus fields north of the Canary Islands in June/July 1997 [*Brenguier et al.*, 2000]. The CASI is a "push-broom" imaging spectrometer with a field of view of 34° across the flight track.

[9] *Zinner et al.* [2006] developed a retrieval for three-dimensional cloud structures from the high-resolution 2-D radiance fields. The knowledge of the horizontal photon transport characteristic for each cloud structure was used to compensate for the independent pixel error. The plane-parallel bias is negligible at the observational resolution of

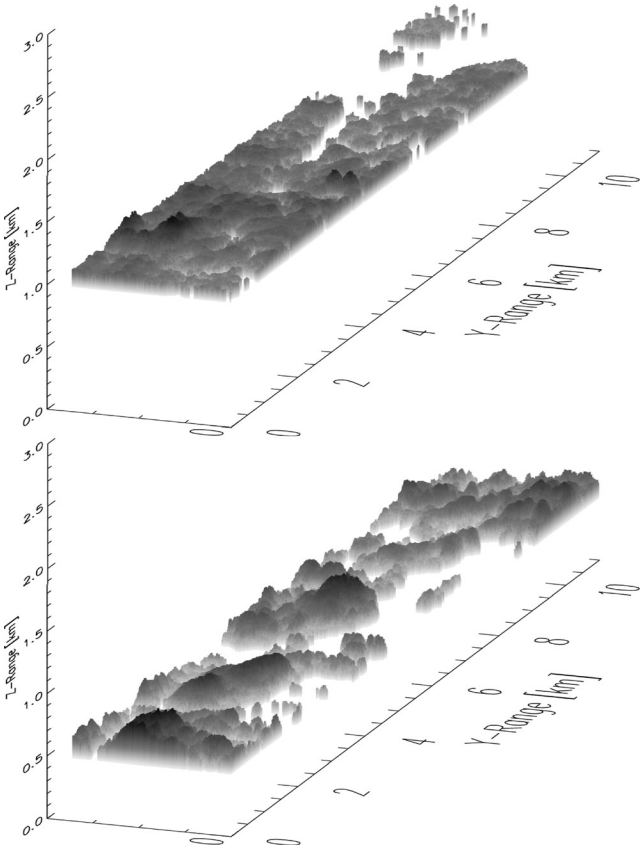

Figure 2. 3D cloud structure for two CASI cases (cf. Figure 1). The grey-scale illustrates the vertical structure of the clouds; increasing LWC and droplet radius with height are indicated by darker grey values [*Zinner et al.*, 2006].

15 m × 15 m because no significant subscale variability of the radiation field has to be expected below this scale which is smaller than the mean free path length of photons between two scattering or absorption events [*Marshak et al.*, 1998a]. An adiabatic model for the increase of cloud droplet size and liquid water content from cloud base to cloud top was applied, on the one hand, to translate a retrieved optical thickness and an in situ droplet number to a cloud geometrical thickness and, on the other hand, to define liquid water content and effective radius in each height level above cloud base. This way cloud structures were retrieved for 27 CASI scenes from the ACE2 CLOUDYCOLUMN data set representing 27 parts of stratocumulus fields. The scenes were selected for certain prerequisites (small solar zenith angle, single layer) favorable for the retrieval (Figure 2). The resulting 3-D cloud structures comprise liquid water content and effective droplet radius within cloud boxes of 15 m × 15 m × 10 m size.

[10] The statistical characteristics (mean and variability) of the data set compare well to measured statistics of marine stratocumulus clouds from several campaigns and thus seem to be representative for marine stratocumulus clouds. The cloud fractions of the 27 scenes were between 5% and 100% (most scenes >30%). The optical thickness τ of the cases ranges from 0 to 40 with an average value of $\bar{\tau} = 9$. The geometrical thickness d was up to 500 m with an average value of $\bar{d} = 146$ m. The effective radius r_{eff} reaches maximum values of 15 μm near cloud top ($\overline{r_{\text{eff}}} = 9.4$ μm at cloud top). The variation of the cloud top height is characterized by standard deviations between 14 m and 71 m depending on the cloud scene.

2.2. Radiative Transfer Model and Simulation of Satellite Sensor Observations

[11] All following radiative transfer simulations were done with the three-dimensional Monte Carlo code for the physically correct tracing of photons in cloudy atmosphere (MYSTIC) [*Mayer*, 1999; *Mayer*, 2000]. MYSTIC is a forward Monte Carlo code which traces photons on their individual paths through the atmosphere. Radiances are calculated using a local estimate technique [e.g., *Davis et al.*, 1985]. In this configuration MYSTIC has been successfully validated in the Intercomparison of 3-D Radiation Codes (I3RC) [*Cahalan et al.*, 2005]. MYSTIC is operated as part of the libRadtran (library of radiative transfer) package [*Mayer and Kylling*, 2005], which prepares the optical properties of the atmosphere, to be used in the model. For this study, molecular absorption was based on LOWTRAN, as adopted from *Ricchiazzi et al.* [1998]. For the simulation of measurements over sea, a Lambertian surface albedo of 2.5% was assumed which is a reasonable assumption outside the sunglint region. Generally, no sunglint effects need to be taken into account below clouds of sufficient optical thickness; in addition, the selection of sun and sensor angles in the following avoids this region almost completely. The cloud microphysical properties (liquid water content and effective droplet radius) were converted to optical properties via Mie calculations. For all calculations a standard atmosphere for midlatitude summer was assumed [*Anderson et al.*, 1986]. To achieve complete consistency, even the calculation of 1-D and IPA radiance was done with MYSTIC in independent-pixel mode for which the horizontal transport of photons between columns is switched off. Although the calculation would be much faster with one of the one-dimensional radiative transfer solvers implemented in libRadtran, like DISORT [*Stamnes et al.*, 1988], we decided against that in order to prevent the result to be disturbed by any differences between solvers.

[12] MYSTIC allows arbitrary simulations of sensor and solar illumination geometries. Typical passive remote sensing cloud sensors are airborne instruments comprising viewing angles close to the nadir direction (e.g., CASI), satellite instruments on a polar-orbit also close to the nadir direction (e.g., TERRA/MODIS or NOAA/AVHRR), or satellite instruments on geostationary platforms with specific observation geometries depending on the geographical location of the image pixel and the time (e.g., Meteosat-8/SEVIRI). Accordingly, two different sensor zenith angles θ_{sen} were simulated: 0° representing near nadir viewing angles and 55° corresponding to the sensor zenith angle of Meteosat-8 for Central Europe. Solar zenith angles θ_{sol} simulated are 0°, 30°, 45°, and 60°, relative solar azimuth angles ϕ_{sol} are 90° (sun perpendicular to the viewing direction), 135°, and 180° (sun in the back of the observer). This way most of the interesting constellations for sensors viewing midlatitudes were covered by simulations.

[13] The horizontal resolution of the original CASI observations of 15 m × 15 m (Figure 1) was chosen for cloud

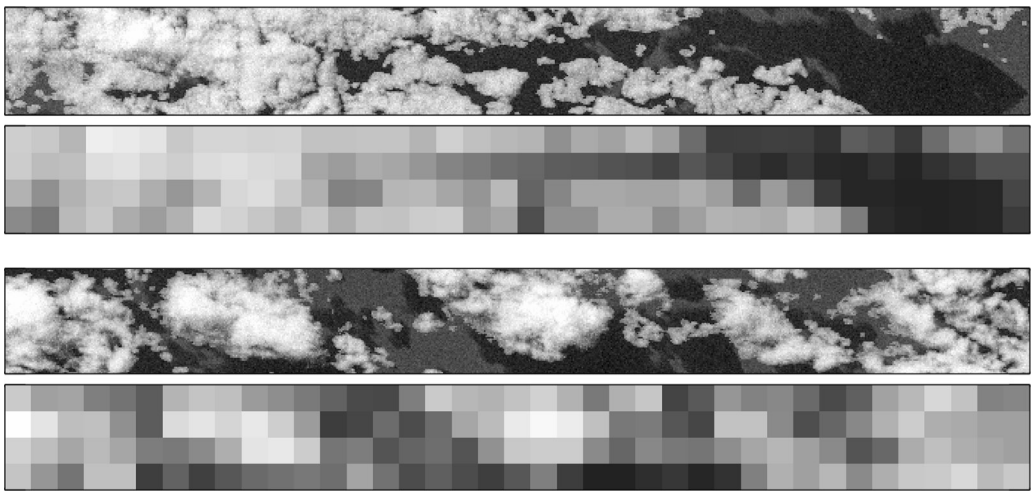

Figure 3. Examples of MYSTIC simulations for the cloud structures of Figure 2 for sensor zenith θ_{sen} = 0°, solar zenith θ_{sol} = 60°, and solar azimuth relative to the top of the picture ϕ_{sol} = 315° in the 830 nm wavelength band. Shown are the maximum (simulation) resolution and a reduced (satellite sensor) resolution.

input (Figure 2) as well as for the radiance output (Figure 3). A vertical resolution of the 10 m was used for the cloud input as well as for the radiative transfer simulations. Subsequently, these fields were averaged to the desired sensor's horizontal resolution: 30 m × 30 m representing a typical pixel size of an airborne or a very high resolution satellite instrument; 990 m × 990 m representing a typical pixel size for polar-orbiting satellite sensors; and the whole scene of 1.3 km × 10 km, approximating an observation from the geostationary perspective with a pixel size between the SEVIRI high (1.33 km × 2 km) and normal resolution (4 km × 6 km) channels for Central Europe.

[14] A 16 processor × 1.4 GHz PC cluster was used for the extensive computations (27 cloud scenes × 10 illumination situations × two wavelength bands). For each individual high-resolution pixel, about 1000 photons had to be traced to reach a standard deviation (Monte Carlo noise) of 5%. The accuracy of radiance values obtained by averaging the results to lower resolutions increases proportional to the square root of the number of photons contributing to the value, i.e., the standard deviation is inversely proportional to the linear pixel size.

2.3. Cloud Retrieval

[15] Focus of this study is a standard cloud property retrieval for the simultaneous determination of optical thickness and effective radius from a combination of a visible and a near infrared channel described by *Nakajima and King* [1990] or *Platnick et al.* [2003]. All mentioned instruments comprise a minimum set of spectral channels in the visible and near-infrared, including two channels at 650 and 830 nm and one near-infrared channel at 1600 or 3700 nm, a combination of which is generally used for cloud remote sensing. One channel is chosen outside the liquid water absorption bands (830 nm). The reflected radiance in this channel depends mainly on the vertically integrated cloud optical thickness. The second channel is chosen inside a spectral band including absorption by cloud droplets in addition to scattering effects (1600 nm). As the single scattering albedo strongly depends on the droplet size in this case, the reflected radiance in this channel is a measure of the effective radius.

[16] Lookup tables were constructed for all 10 combinations of sun and sensor geometries, containing pairs of optical thickness and effective radius and the corresponding radiance pairs. As described above, these calculations were done with MYSTIC, assuming plane-parallel, vertically and horizontally homogeneous clouds. Radiances were calculated for combinations of 70 optical thickness values between 0 and 200 and 22 effective radius values between 4 and 25 μm. The values of cloud properties amply cover the properties occurring within stratocumulus. The calculated combinations were distributed over the whole range of possible combinations in a way to best cover regions of maximum curvature. As an example, Figure 4 shows the reflectivity pairs in the lookup table for solar zenith angle 0° and sensor zenith angle 0°. Each grid point corresponds to one combination of optical thickness and effective radius. In addition to these calculated reflectances, intermediate values are interpolated to result in lookup tables with a step in optical thickness of 0.1 and a step in effective radius of 0.1 μm. The influence of the Monte Carlo noise in the simulation results is detectable at the highest values of optical thickness but the influence of such minor fluctuations on mean results is negligible as (not shown) tests of the retrieval confirm.

[17] For each pair of measured radiances at 830 and 1600 nm the precalculated lookup tables are searched for the combination of optical thickness and effective radius best matching the observations. For this purpose the following cost function Q is minimized:

$$Q = \left(\frac{R_{830,\mathrm{t}} - R_{830,\mathrm{m}}}{R_{830,\mathrm{m}}}\right)^2 + \left(\frac{R_{1600,\mathrm{t}} - R_{1600,\mathrm{m}}}{R_{1600,\mathrm{m}}}\right)^2 \qquad (1)$$

The subscript "t" labels the precalculated reflectivity at 830 or 1600 nm in the lookup table, the subscript m the measured values. The minimum is determined by simply

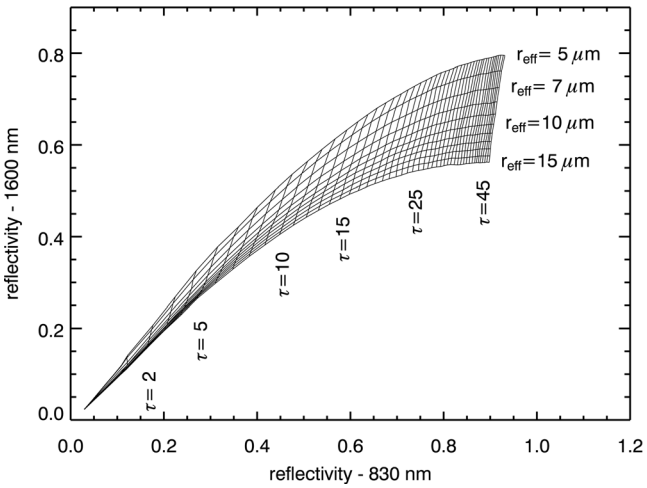

Figure 4. MYSTIC simulated nadir reflectivity ($\theta_{sen} = 0°$) for plane-parallel clouds comprising values of optical thickness $0 \leq \tau \leq 50$ and effective radius $5 \leq r_{eff} \leq 15$ for a solar zenith angle $\theta_{sol} = 0°$.

testing all pairs in the lookup table, a computationally expensive but safe method to find the absolute minimum.

2.4. Definition of Error Quantities

[18] In this section the two sources of uncertainty of passive remote sensing methods due to cloud inhomogeneity are examined in more detail and a definition of errors is given allowing to separate the two contributions, the plane-parallel bias and the independent pixel error.

[19] The lack of information on subpixel resolution inhomogeneity leads to the plane-parallel bias caused by the nonlinear relationship between cloud optical thickness and reflectivity (Figure 5). The sign of the bias depends on the specific character of the nonlinearity in the range of interest and on the range of the neglected unresolved inhomogeneity. In the largest part of the optical thickness range displayed in Figure 5 the retrieval would underestimated the true average optical thickness. However, for small optical thickness the opposite effect is possible as well. Owing to surface reflection and scattering in the background atmosphere, the reflectivity is already nonzero even for zero cloud optical thickness which leads to curvatures causing an overestimation of the optical thickness. The plane-parallel bias tends to increase with pixel size and the accordingly increasing inhomogeneity. For the retrieval of the optical thickness, the considerations of Figure 5 hold equivalently for a two channel retrieval as the dependence of the reflectivity on the optical thickness is qualitatively the same for both channels.

[20] If pixels are smaller than the mean free path length of photons, they no longer contain any unresolved inhomogeneity with impact on the radiation field [*Marshak et al.*, 1998a]. Nevertheless, the independent pixel assumption still constitutes an independent source of error. A pixel's reflectivity does not only reflect pixel characteristics but also characteristics of the surrounding. The neglect of net horizontal photon flux between adjacent pixels causes the independent pixel uncertainty. On the one hand the horizontal transport of photons can smooth the reflectivity distribution, on the other hand geometrical effects like shadows and bright slopes can lead to roughening (or sharpening [*Marshak et al.*, 1998a; *Loeb et al.*, 1998]. This effect is strongest for high resolution (small pixel size) where the pixels cannot be assumed independent.

[21] For the analysis we split the total retrieval error due to cloud inhomogeneity $\Delta\tau_{tot}$ into these two parts, plane-parallel and independent pixel error ($\Delta\tau_{pp}$ and $\Delta\tau_{ip}$), in a way that $\Delta\tau_{tot} = \Delta\tau_{ip} + \Delta\tau_{pp}$. Let us formally write the retrieval procedure as a function f applied to the observed reflectivity R. Then the retrieved optical thickness τ_{ret} is simply $\tau_{ret} = f(\overline{R})$ where $\overline{R}$ is the reflectivity averaged over one pixel. Owing to the neglect of horizontal photon transport and missing knowledge about subpixel inhomogeneity, τ_{ret} will differ from the actual (pixel averaged) optical thickness $\overline{\tau_{real}}$. The total error of the pixel's retrieved value is therefore

$$\Delta\tau_{tot} = \tau_{ret} - \overline{\tau_{real}}. \tag{2}$$

A perfect retrieval would have to be based on a single hypothetical value of plane-parallel reflectivity independent from the surrounding (R_{ip}). Let us for a moment assume that net horizontal photon flux could be neglected, that is, that the hypothetical independent pixel reflectivity R_{ip} equals the actual reflectivity. Thus we could retrieve the real optical thickness of a pixel $\overline{\tau_{real}}$ without error if we could consider the subpixel contributions of the independent-pixel reflectivity R_{ip} separately:

$$\overline{\tau_{real}} = \overline{f(R_{ip})}. \tag{3}$$

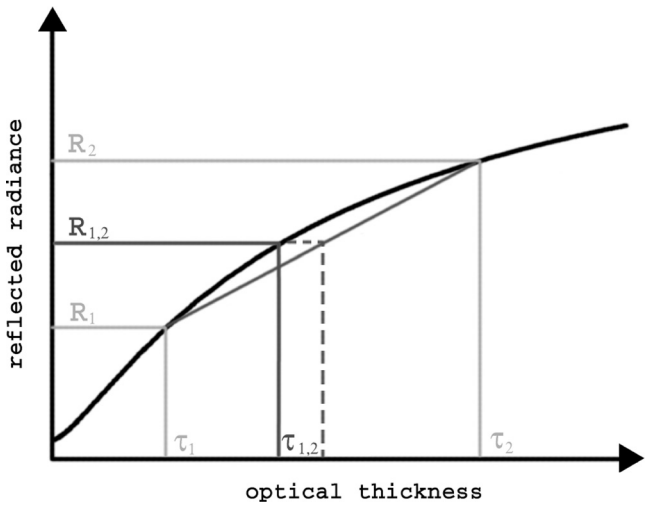

Figure 5. Relationship between optical thickness and reflected radiance. Averaging the values of reflectivity R_1 and R_2 to the mean value of $R_{1,2}$ due to limited resolution leads to a retrieved optical thickness $\tau_{1,2}$ which is too small compared to the value $(\tau_1 + \tau_2)/2$ retrievable if R_1 and R_2 were known.

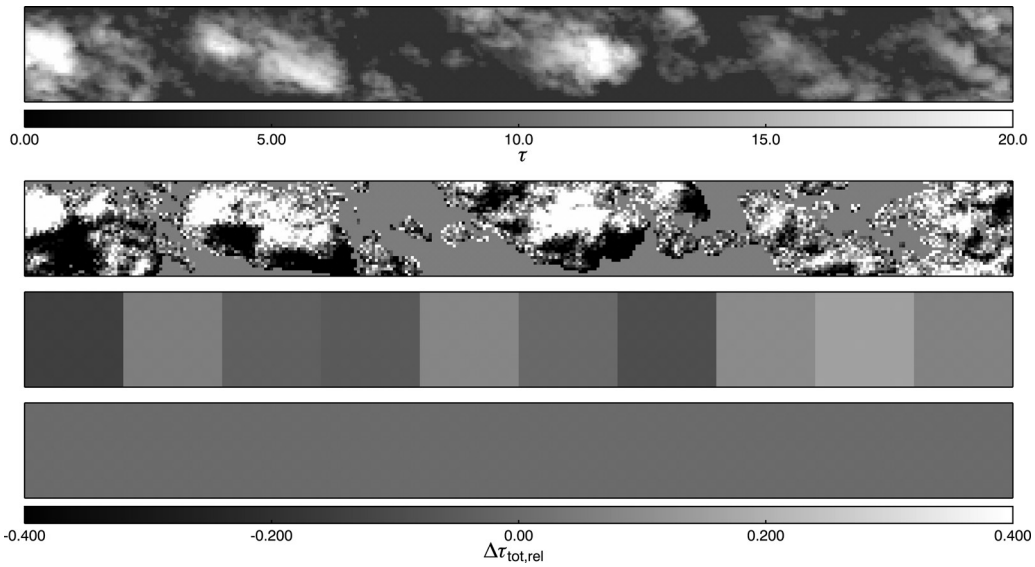

Figure 6. Error analysis example case. From top to bottom: field of real optical thickness (compare Figures 1, 2, and 3), relative total bias for solar zenith $\theta_{sol} = 60°$ and solar azimuth relative to the top of the picture $\phi_{sol} = 315°$ for high 30 m resolution sensor (nadir view), for 1 km resolution "polar-orbiting" sensor (nadir view), and for 13 km^2 resolution "geostationary" sensor (sensor zenith 55).

As we do not know these details but only the pixel average reflectivity $\overline{R_{\mathrm{ip}}}$, the remaining retrieval error would only be due to the plane-parallel bias:

$$\Delta\tau_{\mathrm{pp}} = f\left(\overline{R_{\mathrm{ip}}}\right) - \overline{f\left(R_{\mathrm{ip}}\right)}. \tag{4}$$

That means we cannot retrieve the true value $\overline{f\left(R_{\mathrm{ip}}\right)}$ but only the biased $f(\overline{R_{\mathrm{ip}}})$.

[22] In the second step of our error separation we now have to account for the uncertainty caused by any horizontal photon transport, that is, by the difference between the retrieval of optical thickness based on the actual reflectivity $\overline{R}$ and based on the hypothetical independent pixel reflectivity $\overline{R_{\mathrm{ip}}}$ for each pixel:

$$\Delta\tau_{\mathrm{ip}} = f\left(\overline{R}\right) - f\left(\overline{R_{\mathrm{ip}}}\right). \tag{5}$$

To be precise, this error component describes the impact of any 3-D photon transport, between the pixels as well as within the pixels. This way it becomes technically possible to separate inhomogeneity and 3-D photon transport effects. If we add both and remember that $\tau_{\mathrm{ret}} = f(\overline{R})$, we find that the sum of the components $\Delta\tau_{\mathrm{pp}}$ and $\Delta\tau_{\mathrm{ip}}$ is just the total error.

[23] In our model world we can calculate all involved quantities the true 3-D radiative transfer reflectivity R and the hypothetical reflectivity independent from 3-D radiative transport R_{ip} which allows us now to separate the total error into its components.

[24] In the following, errors are mostly presented as averages over several pixels (binned into certain classes), relative to the true optical thickness $\overline{\tau_{real}}$:

$$\Delta\tau_{\mathrm{x,rel}} = \frac{\sum_i \Delta\tau_{\mathrm{x},i}}{\sum_i \left(\overline{\tau_{\mathrm{real}}}\right)_i}. \tag{6}$$

Here "x" represents the subscripts "ip," "pp," and "tot," "$\sum_i$" is the sum over all pixels of a class. Statistical properties given (standard deviation, percentiles) are always statistics of relative values.

3. Results

[25] In this section the uncertainties and biases of the remote sensing results caused by the cloud inhomogeneity are quantified. The basis is the remote sensing technique described in section 2.3. The focus is laid on the analysis of retrieved optical thickness compared to the true optical thickness (section 3.1). The retrieval of effective radius is also examined, but here the evaluation is not as straightforward, owing to general difficulties in interpreting satellite derived effective radii (see section 3.2).

3.1. Optical Thickness

[26] As outlined in section 2.2, each analysis is carried out for 10 different sun-satellite-geometries reflecting typical daylight situations and for three different spatial resolutions reflecting nadir viewing sensors of different resolution as well as a low-resolution geostationary sensor. For an example case see Figure 6.

3.1.1. High Resolution

[27] The first type of cloud remote sensing instrument inspected is a very high resolution air- or satellite-borne imager with a pixel size of 30 m × 30 m. By averaging the maximum resolution (15 m) reflectivities the standard deviation (Monte Carlo noise) of the simulated values at this resolution is reduced by a factor of 2 to about 2.5%. As the only sensor viewing direction analyzed for this type of sensor is the nadir view, the different solar azimuth angles are not treated separately.

[28] Figure 7 shows the independent pixel error $\Delta\tau_{\mathrm{ip\ rel}}$, the plane-parallel bias $\Delta\tau_{\mathrm{pp\ rel}}$, and the total error $\Delta\tau_{\mathrm{tot\ rel}}$ relative to the true optical thickness of each 30 m × 30 m cloud element as a function of the true optical thickness.

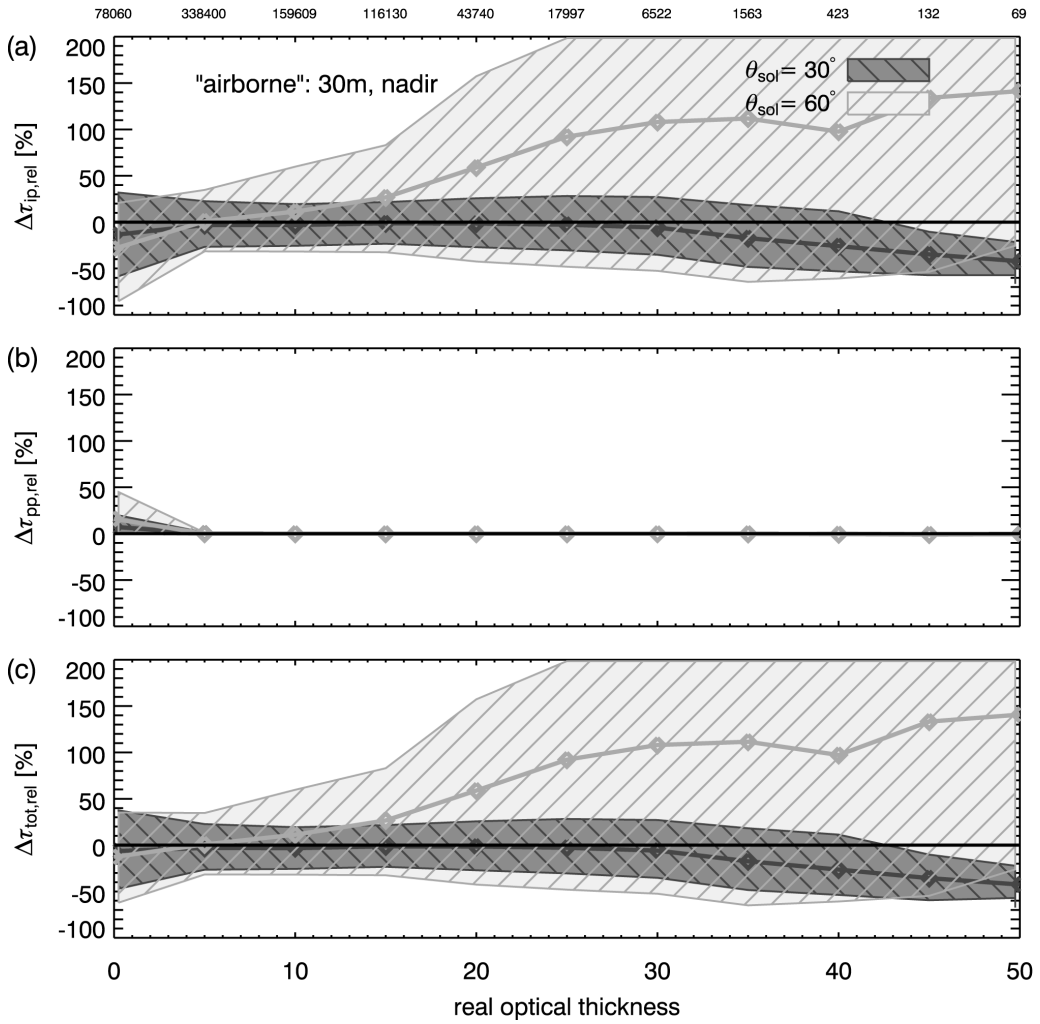

Figure 7. Error analysis for a nadir viewing 30 m horizontal resolution sensor for all 27 cases for two of the four solar zenith angles (30°, 60°; solar azimuth angles are not separated): Thick lines give the bias depending on the real optical thickness, the shaded regions give the spread of single pixel's errors (10% and 90% percentiles). Values are binned into optical thickness intervals (0–2.5, 2.5–7.5, 7.5–12.5, . . .) and averaged. The bin average values are marked by a diamond symbol. The number of pixels in each bin is given on top of the figure. (a) The independent pixel contribution $\Delta\tau_{ip\ rel}$, (b) the plane-parallel $\Delta\tau_{pp\ rel}$, and (c) is the sum of both, the total relative error $\Delta\tau_{tot\ rel}$.

Cloud-free 30 m pixels ($\tau < 0.1$) are excluded from the analysis. For reasons of presentation only two values of solar zenith angle are depicted. Shown are mean values of the error for all 30 m pixels in the 27 cloud data sets as well as the spread of errors for single pixel values (10% and 90% percentiles).

[29] It is obvious that at this resolution the total error (Figure 7c) is dominated by the independent pixel error (Figure 7a). The effects of horizontal photon transport are apparent: For small solar zenith angle the optical thickness is underestimated compared to the real values; for large solar zenith angles the optical thickness is strongly overestimated (mean deviations are marked by the thick solid lines). These effects were discussed in literature before, and *Davis and Marshak* [2001] call the effect "channeling." In the first case the horizontal transport of photons leads to an increase in transmission of radiation over the whole scene. For small solar zenith angles, radiation is transported in the horizontal, away from the highly reflective optically thick parts of the cloud to the less reflective optically thinner or even cloud free parts where more photons are transmitted through the cloud. The dependence of the independent pixel error on the true optical thickness further illustrates the effects. Optically thick regions loose reflectivity, compared to the IPA, while optically thin regions at least partially gain reflectivity leading to corresponding error in the retrieval. As the solar zenith angle increases, this effect is compensated by an opposite effect (compare also Figure 6). The effective cloud cover exposed to the incident solar radiation increases. This is not only true for broken cloud scenes: Generally, the top parts of the clouds which are optically thicker are preferably illuminated (remember that optical thickness and cloud top height are directly related due to the assumption of adiabatic increase of the liquid water content with height). Radiation from the sun enters these parts not only through the cloud top as assumed for the independent

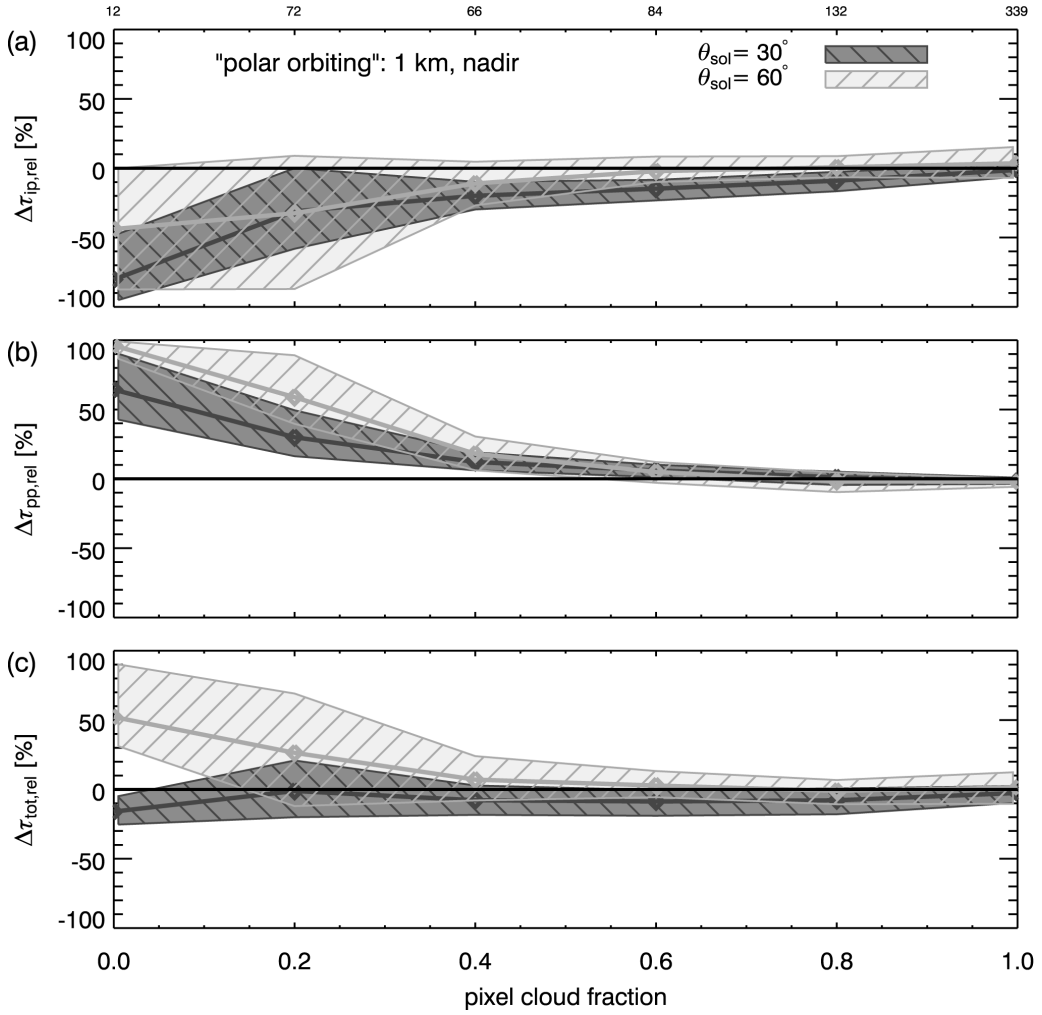

Figure 8. Error analysis for a nadir viewing 990 m horizontal resolution sensor for all 27 cases for two of the four solar zenith angles (30°, 60°; solar azimuth angles are not separated): As Figure 7 but values are binned into intervals of pixel cloud fraction (0–0.1, 0.1–0.3, 0.3–0.5, ...) and averaged.

pixel approximation but through the cloud sides as well. Thus more radiation is reflected upwards and on average a higher optical thickness is retrieved for the scene. Shadows and bright slopes lead to a further overestimation of the retrieved average optical thickness due to the relationship between optical thickness and cloud reflectivity as depicted in Figure 5. An increase of radiation on the illuminated slope (e.g., R_2 in Figure 5) enhances the retrieved value of optical thickness more than the smaller reflectivity on the shadowed slope reduces it (e.g., R_1). The uncertainty for single pixels reaches several hundred percent on this resolution (shaded area in Figure 7a). For the mentioned reasons, the uncertainty is not random. Rather, a large bias occurs, ranging between 40% underestimation and 140% overestimation due to the neglect of horizontal photon transport.

[30] The plane parallel error (Figure 7b) is small as suspected for this resolution in section 2.1. Cloud inhomogeneity below the 30 m resolution is hardly affecting the variability of the radiation field. Just for the smallest cloud optical thickness some deviation occurs. Only at these small cloud optical thickness both kinds of plane parallel error can occur, the positive and the negative. As the plane-parallel error is minimal the total relative errors in optical thickness (Figure 7c) is clearly dominated by the independent pixel error.

3.1.2. Typical Polar-Orbiting Sensor Resolution

[31] The same kind of near nadir viewing directions is typical for the polar-orbiting standard of cloud remote sensing. Sensors like AVHRR, MERIS, or MODIS obtain measurements of reflectivity on resolutions between several 100 m and 1 km pixel size. Here the most common cloud products resolution of 1 km is investigated in detail. It is simulated by averaging of 66 × 66 pixels of the Monte Carlo simulations of section 2.2. The standard deviation (Monte Carlo noise) of the results at this 990 m pixel size is smaller than 0.1%.

[32] Compared to the high-resolution sensor in the preceding section, not only the horizontal photon transport but also the subscale inhomogeneity is of importance at this resolution which is clearly illustrated by Figure 8. In contrast to Figure 7 the relative errors are plotted versus the 990 m pixel's cloud fraction which seems to be the more relevant quantity.

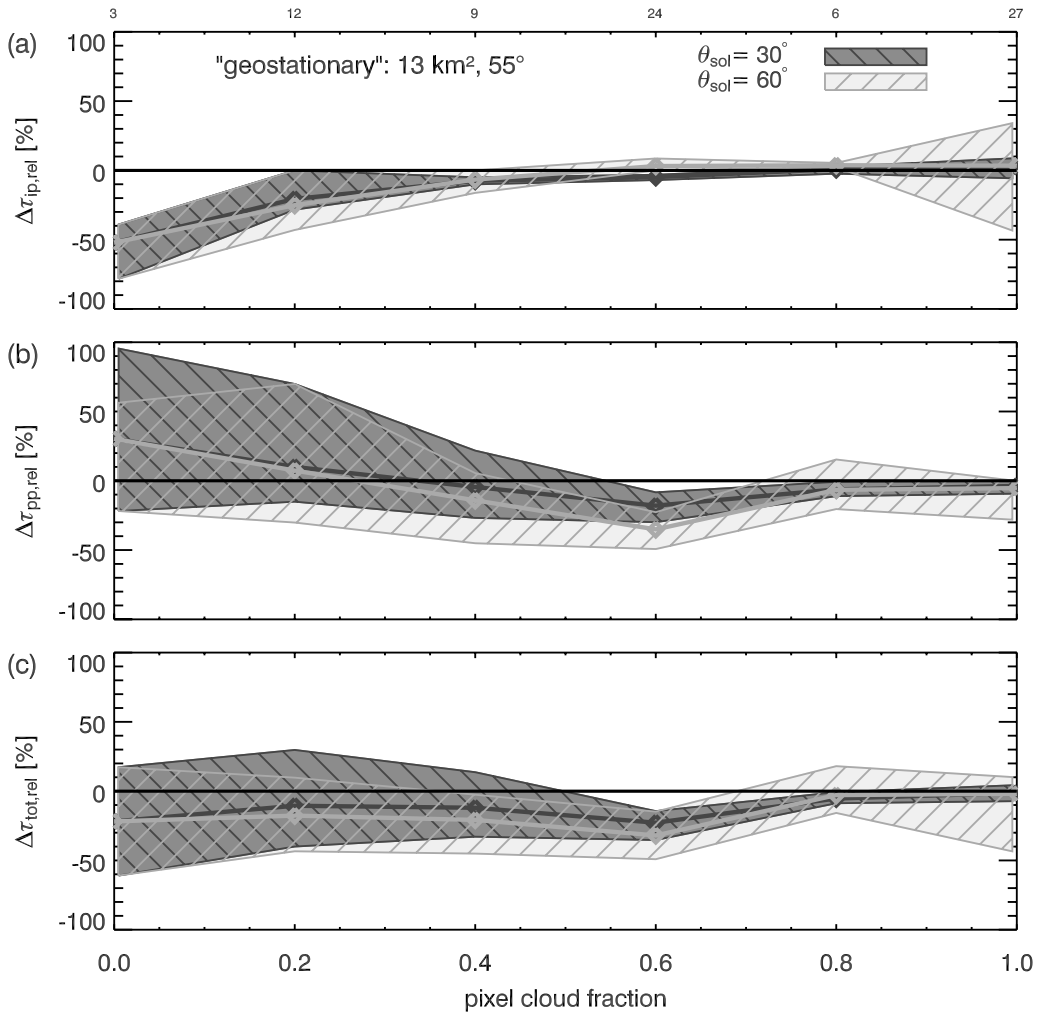

Figure 9. Error analysis for a sensor with pixel size of about 13 km^2 and a sensor zenith angle $\theta_{sen} = 55°$ for all 27 cases for two of the four solar zenith angles (cf. Figure 8).

[33] Compared to the deviations in the case of airborne high-resolution remote sensing (Figure 7a), the independent pixel error is reduced at 1 km pixel size (Figure 8a). It depends clearly on the cloud cover. The horizontal transport of photons and thus the diffusion of photons through cloud gaps affects a pixel's reflectivity the stronger the lower the pixel cloud fraction is. Geometrical effects start to become effective for large solar zenith angles and again compensate the first effect, but in contrast to the 30 m resolution this effect is much smaller. The reason is that at 1 km resolution bright and shaded slopes may now occur in one and the same pixel which reduces their impact considerably (see Figure 6). This is in contrast to the high resolution where bright and shaded areas usually appear in separate pixels. Hence not only the mean errors are reduced but also the spread of individual pixel's error when the pixel size is increased.

[34] As expected, the deviations due to the plane-parallel error are larger as 990 m pixels contain a distinctively inhomogeneous reflectivity distribution (Figure 8b). The plane-parallel error is negative for the largest pixel cloud fraction, i.e., for large optical thickness. For smaller cloud fraction the impact of the opposite curvature effect for small optical thickness becomes effective. The bias is smallest for all solar zenith angles if the pixel is completely overcast, i.e., most homogeneous.

[35] Interestingly, in a large part the two error components do cancel each other out at this resolution. Most notably this effect is visible for 30° solar zenith angle, were large independent pixel underestimations of −20 to −80% for partially covered pixels are compensated for by a large plane-parallel error of the opposite sign and similar magnitude to result in much smaller total biases (−10 to −20%).

[36] The total bias of remote sensing of the optical thickness of partially covered pixels for the 1 km resolution (Figure 8c) ranges between −20 and +50% at maximum depending on solar zenith angle. For overcast pixels the bias is almost zero. However, the bias increases for cloud fractions smaller than 1. Hence if the complete coverage of a pixel cannot be guaranteed (which is often the case for remote sensing data), a relatively large uncertainty must be assigned to the pixel. Even for a pixel with a relatively large cloud fraction between 0.7 and 0.9, the optical thickness for a solar zenith angle of 30° is already underestimated by about 10% on average. Remote sensing results for single pixels are much more uncertain: The shaded region in

Figure 8c containing 80% of all pixels (10% and 90% percentiles) illustrates that single data points, even for completely covered pixels, are often in error by ±20%. The reason for this uncertainty are the three-dimensional effects (Figure 8a).

[37] In order to be precise, the standard polar-orbiting sensors do not only observe the reflectance for the nadir direction but for larger viewing angles as well. The analysis for a viewing angle of 55° is not shown here but was performed as well and does not lead to substantially other magnitudes of uncertainty values or other conclusions.

3.1.3. Typical Geostationary Resolution

[38] Apart from the much larger pixel size typical for sensors on geostationary satellites, these have very distinct viewing characteristics depending on the geographical location of the region under investigation. Distinct effects are to be expected especially for high latitudes at which geostationary satellite sensors are still widely used (Northern/Central Europe, North America), for example, to derive cloud climatologies. Our main area of interest are clouds over Central Europe over land and sea observed from the Meteosat-8 satellite. There a typical geostationary observation geometry would be a relatively oblique sensor zenith of 55° with the sun "in the back" of the sensor. In contrast to the nadir observations studied above, the relative azimuth between sun and satellite needs to be considered. Figure 9 shows a summary of the results, as in the previous sections. The peculiarities of this viewing geometry for special combinations of solar zenith and azimuth angles are discussed with the help of Table 2 later on. As the number of available pixels is rather small (one scene is only one pixel), the error spread needs to be obtained in a slightly different way: If less than 10 pixels are found in one class of pixel cloud cover, the minimum and maximum values instead of the 10% and 90% percentiles are plotted.

[39] The independent pixel uncertainty is further reduced on this resolution (Figure 9a). Biases are small, already for a pixel cloud cover larger than 0.4; the spread of errors is much smaller than for the other sensor settings. Only for a cloud cover close to 1, the uncertainty is high for 60° solar zenith angle. Here the retrieval is based on the reflectivity for a viewing angle close to the 180° backward scattering ($\theta_{sen} = 55°$, $\theta_{sol} = 60°$, $\phi_{sol} = 180°$). In this angular region any reflected radiance is affected by the backscatter glory [*Mayer et al.*, 2004]. This single scattering phenomenon is sensitive to the effective radius at cloud top even outside water absorption bands (i.e., 830 nm). Therefore ambiguities appear in the retrieval as both channels become similarly sensitive to effective radius. Only for completely covered scenes with a rather uniform geometrical cloud thickness and effective radius at cloud top those can have a systematic impact as otherwise the glory effect is not characteristic for a certain value of effective radius. Therefore such a large uncertainty is not detected if a large variety of cloud boundary values of effective radius are seen by the sensor as it is the case for broken cloud scenes.

[40] As expected the plane-parallel error further increases for the large 13 km^2 pixels. In contrast to the sensors with higher resolution, the plane-parallel error is of considerable magnitude not only for small but also for larger cloud fractions, clearly negative up to the fully covered pixel class where one can still see a bias of around −5%.

[41] A negative bias of −10% to −20% occurs up to cloud fraction of 0.8. Only for overcast pixels the bias almost vanishes. The spread of individual pixel errors is of similar size as for the 1 km × 1 km resolution: 20–50%.

3.2. Effective Radius

[42] The uncertainties of the retrieval of the effective radius is more difficult to investigate than the optical thickness. The retrieval of the effective radius is based on the liquid water absorption at near infrared wavelengths (1.6 μm), and due to this absorption it is only representative of a certain penetration depth into the cloud. *Nakajima and King* [1990] found the value of effective radius which can be retrieved for a layered cloud to be of 85–95% of the value at cloud top. This value depends of course on the profile of the effective radius. In contrast to the cloud optical thickness the effective radius is not defined for cloud free areas and thus it is not easy to find sensible "true" values for partially covered pixels. Hence even for an ideal plane-parallel cloud there is no simple value to compare with. Also, the reflectivity at 1.6 μm is determined by both optical thickness and effective radius. Any uncertainties and biases in the retrieval of optical thickness at the same time influence the retrieved effective radius much stronger than the other way round.

[43] Because of those points the following analysis of the inhomogeneity influence is simplified and only completely cloud covered pixels are investigated. The definition of a basis value, the "truth," as a starting point of the analysis is the first task to be addressed. The situation without inhomogeneity or 3-D radiative transfer influence is approximated by independent pixel simulations for a selection of typical cloudy columns (a random choice of 1000 columns from all cloudy columns within the set of 27 cloud structures) and a successive application of the retrieval to the results of these simulations. This way an estimation of the retrievable values of effective radius excluding any 3-D effect is found. The results of this preinvestigation are shown in Table 1. The relative deviation of the retrieved effective radius from the given values at cloud top are given for the investigated viewing angles and solar illumination angles. Typically, there are underestimations of the cloud top values between 10 and 15%, matching the results of *Nakajima and King* [1990]. Within the investigated cloudy columns such values are typically reached about 40 m below cloud top equivalent to an optical penetration depth of $\tau = 4$. Again, the only exception is the angular region of the glory phenomenon close to the 180° backward scattering ($\theta_{sen} = 55°$, $\theta_{sol} = 60°$, $\phi_{sol} = 180°$) where the retrieval is based on the reflectivity. The glory obviously leads to a retrieval of effective radius values more representative of the cloud top as the reflectivity is affected by single scattering there [*Mayer et al.*, 2004].

[44] The basis values found this way can now be compared to the results for a retrieval applied to the full 3-D field of reflectivity. Table 1 shows the mean deviations of the retrieved values of effective radius for the typical polar-orbiting and geostationary sensor resolutions. In contrast to Table 1 values of 90 to 95% of the cloud top values of effective radius are reached. Thus it can be stated that for completely cloudy pixels an overestimation of about 5% compared to independent pixel investigations has to be

Table 1. The "truth" Section Gives the Values of Effective Radius as Deviations (in Percent) From Radius at Cloud Top Expected Without 3-D Radiative Transfer and Cloud Inhomogeneity, the 3D Section Gives the Values Taking Into Account 3-D Radiative Transfer and Cloud Inhomogeneity[a]

	Solar Zenith	0°	30°			45°			60°		
	Solar Azimuth	–	90°	135°	180°	90°	135°	180°	90°	135°	180°
"Truth"	polar-orbiting	−12.0 (8.2)	−13.9 (9.2)	−13.8 (9.7)	−12.6 (9.1)	−14.1 (10.2)	−14.8 (10.2)	−14.4 (11.1)	−11.3 (8.3)	−11.6 (8.8)	−11.4 (8.7)
	geostationary	−11.1 (11.8)	−10.4 (12.2)	−11.3 (13.3)	−10.4 (11.2)	−10.9 (12.3)	−11.5 (14.5)	−7.0 (8.8)	−9.4 (12.7)	−9.5 (13.5)	−0.3 (16.2)
3-D	polar-orbiting	−10.6 (5.8)	−8.7 (6.4)	−8.6 (6.0)	−8.0 (4.5)	−9.6 (10.8)	−9.3 (10.7)	−10.2 (8.7)	−8.2 (12.0)	−8.8 (11.7)	−9.3 (9.0)
	geostationary	−7.5 (4.5)	−5.5 (6.3)	−7.3 (7.4)	−8.5 (4.7)	−4.9 (7.4)	−7.6 (8.0)	−6.6 (2.5)	−2.4 (7.6)	−7.2 (5.6)	−18.5 (21.1)

[a]The deviations are separated for solar illumination situations and two different sensor settings. The polar-orbiting (990 m pixel size, nadir view) and the geostationary (13 km^2, 55° sensor zenith). Numbers in brackets give the standard deviation.

expected due to cloud inhomogeneity and 3-D radiative effects. Consequently, the region of the cloud for which the retrieved value is representative is closer to the cloud top.

[45] A possible explanation for such an overestimation could be the reduction of the 1600 nm reflectivity due to inhomogeneity as discussed for the optical thickness retrieval resulting in the retrieval of larger values of effective radius. The small magnitude of errors could be a sign of the reduced independent pixel uncertainty caused by reduced photon path lengths in the absorbing channel. Anyhow, it is difficult to give general explanations for the small deviations in the effective radius retrieval because of the complex twofold dependency on the absorbing and nonabsorbing channels and the large variety of possible effects.

4. Summary

[46] In this investigation the uncertainties of current standard remote sensing techniques, which are based on the assumption of homogeneous cloud properties within a pixel and the neglect of horizontal photon transport, were assessed with respect to real clouds inhomogeneity. Twenty-seven high-resolution three-dimensional cloud structures of marine stratocumulus [*Zinner et al.*, 2006] were the basis of this investigation. Using a three-dimensional Monte Carlo radiative transfer code observations by typical satellite instruments were simulated. A standard remote sensing method was applied to these synthetic observations to retrieve optical thickness and effective radius of the cloudy areas from the reflected radiance in channels with and without liquid water absorption. The results of the retrieval were then compared to the given cloud "truth."

[47] Three different cloud sensor settings have been analyzed: (1) A high 30 m resolution nadir viewing sensor (e.g., airborne sensors, ASTER, Landsat TM); (2) a 1 km resolution standard polar-orbiting satellite type of sensor (MODIS, AVHRR) with viewing angles close to nadir; and (3) a sensor typical for geostationary platforms (GOES, Meteosat) with a resolution of 13 km^2 with a viewing angle typical of midlatitudes. Table 2 gives an overview of the mean pixel bias and standard deviations of optical thickness separately for all simulated sensor settings and for all combinations of viewing and illumination geometries regardless of their cloud fraction. A graphical representation of the errors depending on the pixel size is shown in Figure 10.

[48] Single pixel values for the 30 m resolution nadir viewing sensor do not have sensible physical meaning, unless the retrieval accounts for the horizontal photon transport which is of high importance at this resolution [e.g., *Zinner et al.*, 2006]. For the investigated standard methods the uncertainty easily exceeds 100% for low sun. Nonetheless, the bias over a large number of pixels is small unless the solar zenith angle is high. That means that by excluding the plane-parallel bias through sufficiently small pixel size and the mitigation of the independent pixel uncertainty through averaging it is possible to retrieve rather accurate values of optical thickness.

[49] For the larger pixel size around 1 km × 1 km the neglect of subpixel inhomogeneity produces an uncertainty comparable to that caused by horizontal photon transport which, however, is reduced compared to the high-resolution

Table 2. Relative Bias of the Retrieved Optical Thickness Over All Analyzed Pixel in Percent; Separated for Solar Illumination Situation and Three Different Sensor Settings: Airborne (30 m Pixel Size, Nadir View), Polar-Orbiting (990 m, Nadir View), Geostationary (13 km^2, 55° Sensor Zenith); Numbers in Brackets Give the Standard Deviation

Solar zenith	0°	30°			45°			60°		
Solar azimuth	–	90°	135°	180°	90°	135°	180°	90°	135°	180°
Airborne	−1.7 (23.1)	−3.0 (26.5)	−3.0 (27.2)	−2.4 (26.2)	0.8 (46.2)	0.7 (44.0)	1.6 (48.9)	32.1 (205.2)	25.6 (175.4)	28.4 (180.2)
Polar-orbiting	−5.9 (8.0)	−4.5 (11.5)	−4.2 (10.8)	−3.6 (8.7)	−3.8 (14.7)	−3.4 (13.5)	−2.8 (10.8)	0.9 (21.5)	0.4 (21.7)	3.0 (22.4)
Geostationary	−0.5 (4.3)	−3.9 (7.2)	−9.0 (9.4)	−5.3 (6.8)	−6.5 (9.8)	−9.9 (8.3)	−3.1 (11.9)	−8.6 (13.9)	−12.0 (15.4)	−3.8 (15.6)

case. Biases for the retrieved values of optical thickness are in the order of ±5% for overcast pixels. Partial pixel coverage typically leads to underestimations of the cloud optical thickness around 10% for moderate solar zenith angles to overestimations of the same order for more oblique solar zenith angles. Individual 1 km pixel values are typically in error for ±20% (overcast pixels) up to ±50% (partially covered pixels). Interesting at this resolution is that not only the independent pixel errors for large zenith angles are strongly reduced compared to the 30 m resolution but also the remaining independent pixel biases are strongly reduced by opposing plane-parallel biases (see Figure 8). Both effects contribute to a minimum in total bias and uncertainty at this resolution compared to smaller and larger pixel size visible in Figure 10.

[50] For the geostationary setting of a sensor zenith angle of 55° and a pixel size of 13 km^2, the pixel cloud fraction is of decisive importance. Completely covered pixel's optical thickness can be retrieved with a small bias of only ±3%; for partially covered pixels the retrieved values are typically underestimated by 20% and more (cloud fraction <0.7). Again a single pixels value is burdened with an additional uncertainty of ±20%. The results for the geostationary perspective show decreasing uncertainty but larger biases for most illumination geometries. These are dominated by the increasing plane-parallel bias for this pixel size. For large sensor zenith angle a distinct dependency on the relative solar azimuth can be seen (Table 2). This dependency is determined by the specific plane-parallel error contribution, strongly depending on the character of the retrieval nonlinearity related to these angle combinations. The independent pixel assumptions influence on this resolution is small. Even for the special situation of the sun in the back of the sensor (relative solar azimuth 180°, solar zenith 60°) the positive independent pixel bias is outweighed by the negative plane-parallel bias.

[51] The influence on the values of effective radius retrieved at the same time was also investigated. For this quantity the impact of inhomogeneity and 3-D radiative transfer is hard to separate from several other uncertainties. It was found that on average an increase of effective radius can be found with respect to values which would be retrieved without inhomogeneity and 3-D effects for cloud covered pixels: The typical size of retrieved effective radius under realistic conditions is thus about 90–95% of the values at cloud top compared to 85–90% for the ideal plane-parallel case. This is equivalent to a smaller penetration depth compared to the ideal independent pixel conditions.

5. Conclusions

[52] The large bias due to the independent pixel assumption at very high sensor resolutions is quickly decreasing to moderate values for the standard cloud remote sensing resolutions of polar-orbiting sensors. For typical geostationary sensors and their large pixel sizes the bias increases again, mainly due to the plane parallel error contribution. This finding and the conclusion that a moderate pixel size of about 1 km might be optimal for cloud remote sensing has also been discussed by [*Davis et al.*, 1997; *Varnai and Marshak*, 2001]. Our investigation confirm their findings.

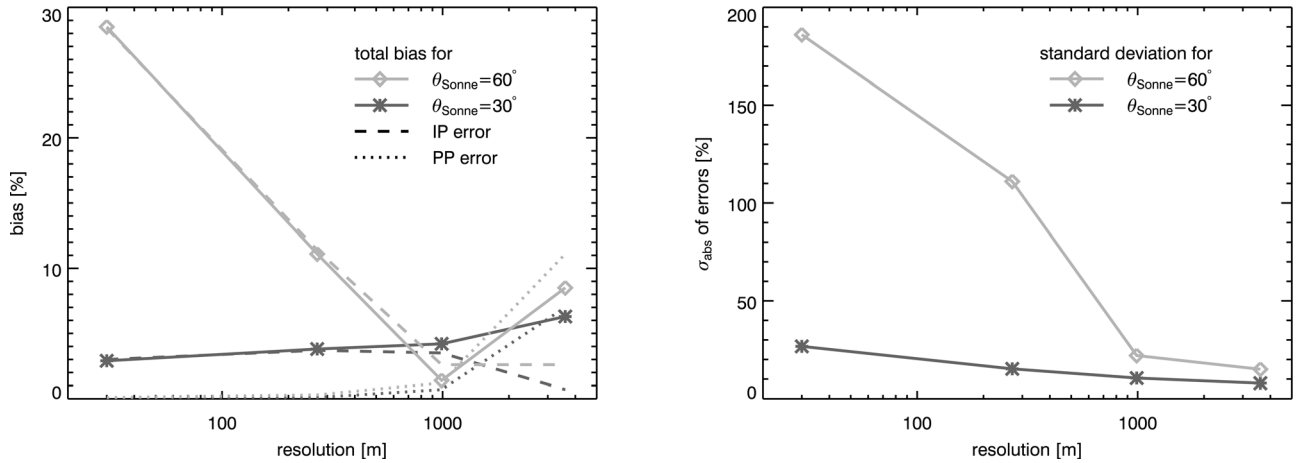

Figure 10. Bias (left) and uncertainty (right) due to cloud inhomogeneity depending on pixel size. The values for the 270 m resolution were not shown in detail in this paper. Displayed are the absolute values of independent pixel bias, plane-parallel bias and total bias as well as the total pixel-level uncertainty for the solar zenith angles 30 and 60° averaged over all solar azimuth angles.

In addition to earlier publications on the general quality of the impact of cloud inhomogeneity on remote sensing results [e.g., *Varnai and Marshak*, 2001], our investigation gives error estimates which are based on stratocumulus cloud structures determined directly from observations. Thus the question of the representativeness of results, closely linked to the underlying cloud data set's "realism," is likely to be addressed in a most appropriate way here.

[53] The central conclusion for cloud remote sensing with typical polar-orbiting or geostationary sensors is that as long as a pixel is completely cloud covered and the solar zenith angle is not too oblique, standard methods work accurately on average. This statement, on the other hand, leads to questions like: How accurate is the classification of sub-pixel-scale cloud cover based on pixel-scale information? Especially for cloud sensors with decreasing resolution an increasing fraction of the pixels is partially covered. For which fraction of all pixels cloud properties are actually obtainable from remote sensing?

[54] In any case, the errors for individual or small numbers of pixels can be much higher. Although most users of remote sensing data might be interested in biases over large areas or data amounts, there are occasions when information for a very limited area is of interest, for example validation campaigns or field experiments. Inhomogeneity effects cause large uncertainties for these situations and require validations to be based on large data sets rather than on individual pixels.

[55] In this context, the effort to provide pixel-level uncertainty information along with standard cloud property products, as the MODIS science team does for their new MODIS "Collection 005" reprocessed products [*Platnick et al.*, 2004; *King et al.*, 2005], is of interest. *Platnick et al.* [2004] investigated the error propagation vom uncertainties in instrument calibration, atmospheric corrections, and albedo into uncertainties of the MODIS cloud property retrievals. For water clouds over ocean and land comprising similar values of optical thickness as the clouds investigated here, they give typical pixel-level uncertainties 5–10%. Uncertainties due to inhomogeneity and 3-D effects are not yet included into this product. Considering the average pixel-level uncertainty of 10–20% found here for a comparable resolution (not to mention biases), an integration of investigation results like the one at hand appears necessary for the future.

[56] **Acknowledgments.** Tobias Zinner was supported by the EC funded CLOUDMAP project, EVK2-2000-00547. The authors thank three anonymous reviewers for their constructive comments.

References

Anderson, G., S. Clough, F. Kneizys, J. Chetwynd, and E. Shettle (1986), AFGL atmospheric constituent profiles, *Tech. Rep. AFGL-TR-86-0110*, Air Force Geophys. Lab., Hanscom Air Force Base, Mass.

Babey, S., and C. Anger (1989), A compact airborne spectrographic imager (casi), in *Proc. IEEE*, *2*, 1028–1031.

Brenguier, J.-L., et al. (2000), An overview of the ACE-2 CLOUDYCOL-UMN closure experiment, *Tellus, Ser. B*, *52*, 815–827.

Bryan, G. H., J. C. Wyngaard, and J. M. Fritsch (2003), Resolution requirements for the simulation of deep moist convection, *Mon. Weather Rev.*, *131*(10), 2394–2416.

Cahalan, R. F., W. Ridgway, W. J. Wiscombe, S. Gollmer, and Harshvardhan (1994), Independent pixel and Monte Carlo estimates of stratocumulus albedo, *J. Atmos. Sci.*, *51*, 3776–3790.

Cahalan, R. F., et al. (2005), The International Intercomparison of 3D Radiation Codes (I3RC): Bringing together the most advanced radiative transfer tools for cloudy atmospheres, *Bull. Am. Meteorol. Soc.*, *86*, 1275–1293.

Davis, A., A. Marshak, R. Cahalan, and W. Wiscombe (1997), The Landsat scale break in stratocumulus as a three-dimensional radiative transfer effect: Implications for cloud remote sensing, *J. Atmos. Sci.*, *54*(2), 241–260.

Davis, A. B., and A. Marshak (2001), Multiple scattering in clouds: Insights from three-dimensional diffusion/P1 theory, *Nucl. Sci. Eng.*, *137*, 251–280.

Davis, J. M., T. B. McKee, and S. K. Cox (1985), Application of the Monte Carlo method to problems in visibility using a local estimate: An investigation, *Appl. Opt.*, *24*(19), 3193–3205.

Di Giuseppe, F., and A. M. Tompkins (2003), Effect of spatial organization on solar radiative transfer in three-dimensional idealized stratocumulus cloud fields, *J. Atmos. Sci.*, *60*, 1774–1794.

Evans, K. F., and W. J. Wiscombe (2004), An algorithm for generating stochastic cloud fields from radar profile statistics, *Atmos. Res.*, *72*, 263–289.

Faure, T., H. Isaka, and B. Guillemet (2001), Neural network retrieval of cloud parameters of inhomogeneous and fractional clouds: Feasibility study, *Remote Sens. Environ.*, *77*, 123–138.

Fu, Q., M. Cribb, H. Barker, S. Krueger, and A. Grossman (2000), Cloud geometry effects on atmospheric solar absorption, *J. Atmos. Sci.*, *57*, 1156–1168.

Iwabuchi, H., and T. Hayasaka (2003), A multi-spectral non-local method for retrieval of boundary layer cloud properties from optical remote sensing data, *Remote Sens. Environ.*, *88*, 294–308.

King, M. D., S. E. Platnick, P. A. Hubanks, G. T. Arnold, G. Wind, and B. Wind (2005), Collection 005 change summary for the MODIS cloud optical property (06_OD) algorithm, in *Collection 005 Change Summary Documents, Level-2 MODIS Atmosphere Products, version 2.2, 14 October 2005*, NASA Goddard Space Flight Cent., Greenbelt, Md. (Available at http://modis-atmos.gsfc.nasa.gov/products_C005update.html).

Loeb, N. G., T. Varnai, and D. M. Winker (1998), Influence of subpixel-scale cloud-top structure of reflectances from overcast stratiform cloud layers, *J. Atmos. Sci.*, *55*, 2960–2973.

Marshak, A., A. Davis, W. Wiscombe, and R. Cahalan (1998a), Radiative effects of sub-mean free path liquid water variability observed in stratiform clouds, *J. Geophys. Res.*, *103*(D16), 19,557–19,567.

Marshak, A., A. Davis, W. Wiscombe, W. Ridgway, and R. Cahalan (1998b), Biases in shortwave column absorption in the presence of fractal clouds, *J. Clim.*, *11*, 431–446.

Mayer, B. (1999), I3RC phase 1 results from the MYSTIC Monte Carlo model, in *Intercomparison of Three-Dimensional Radiation Codes: Abstracts of the First and Second International Workshops*, pp. 49–54, Univ. of Ariz. Press, Tucson, Ariz.

Mayer, B. (2000), I3RC phase 2 results from the MYSTIC Monte Carlo model, in *Intercomparison of Three-Dimensional Radiation Codes: Abstracts of the First and Second International Workshops*, pp. 107–108, Univ. of Ariz. Press, Tucson, Ariz.

Mayer, B., and A. Kylling (2005), Technical note: The libRadtran software package for radiative transfer calculations: Description and examples of use, *Atmos. Chem. Phys.*, *5*, 1855–1877.

Mayer, B., M. Schröder, R. Preusker, and L. Schüller (2004), Remote sensing of water cloud droplet size distributions using the backscatter glory: A case study, *Atmos. Chem. Phys.*, *4*, 1255–1263.

Nakajima, T., and M. D. King (1990), Determination of the optical thickness and effective particle radius of clouds from reflected solar radiation measurements. part I: Theory, *J. Atmos. Sci.*, *47*, 1878–1893.

O'Hirok, W., and C. Gautier (1998), A three-dimensional radiative transfer model to investigate the solar radiation within a cloudy atmosphere. Part I: Spatial effects, *J. Atmos. Sci.*, *55*, 2162–2179.

Platnick, S., M. D. King, S. A. Ackerman, W. P. Menzel, B. A. Baum, J. C. Riedi, and R. Frey (2003), The MODIS cloud products: Algorithms and examples from TERRA, *IEEE Trans. Geosci. Remote Sens.*, *41*, 459–473.

Platnick, S., R. Pincus, B. Wind, M. D. King, M. Gray, and P. Hubanks (2004), An initial analysis of the pixel-level uncertainties in global MODIS cloud optical thickness and effective particle size retrievals, in *Passive Optical Remote Sensing of the Atmosphere and Clouds IV*, vol. 5652, pp. 30–40, SPIE, Bellingham, Wash.

Ricchiazzi, P., S. Yang, C. Gautier, and D. Sowle (1998), SBDART: A research and teaching software tool for plane-parallel radiative transfer in the Earth's atmosphere, *Bull. Am. Meteorol. Soc.*, *79*, 2101–2114.

Rossow, W. B., and R. A. Schiffer (1999), Advances in understanding clouds from ISCCP, *Bull. Am. Meteorol. Soc.*, *80*, 2261–2287.

Scheirer, R., and A. Macke (2003), Cloud inhomogeneity and broadband solar fluxes, *J. Geophys. Res.*, *108*(D19), 4599, doi:10.1029/2002JD003321.

Scheirer, R., and S. Schmidt (2005), CLABAUTAIR: A new algorithm for retrieving three-dimensional cloud structure from airborne microphysical measurements, *Atmos. Chem. Phys.*, *5*, 2333–2340.

Stamnes, K., S. C. Tsay, W. Wiscombe, and K. Jayaweera (1988), A numerically stable algorithm for discrete-ordinate-method radiative transfer in multiple scattering and emitting layered media, *Appl. Opt.*, *27*(12), 2502–2509.

Varnai, T. (2000), Influence of three-dimensional radiative effects on the spatial distribution of shortwave cloud reflection, *J. Atmos. Sci.*, *57*, 216–229.

Varnai, T., and A. Marshak (2001), Statistical analysis of the uncertainties in cloud optical depth retrievals caused by three-dimensional radiative effects, *J. Atmos. Sci.*, *58*, 1540–1548.

Wyser, K., W. O'Hirok, C. Gautier, and C. Jones (2002), Remote sensing of surface solar irradiance with corrections for 3-D cloud effects, *Remote Sens. Environ.*, *80*, 272–284.

Zinner, T., B. Mayer, and M. Schröder (2006), Determination of three-dimensional cloud structures from high-resolution radiance data, *J. Geophys. Res.*, *111*, D08204, doi:10.1029/2005JD006062.

B. Mayer and T. Zinner, Institut für Physik der Atmosphäre, Deutsches Zentrum für Luft- und Raumfahrt, DLR Oberpfaffenhofen, 82234 Wessling, Germany. (tobias.zinner@dlr.de)